High-Resolution ISAR Imaging by Exploiting Sparse Apertures

Lei Zhang, Zhi-Jun Qiao, *Member, IEEE*, Meng-Dao Xing, *Member, IEEE*, Jian-Lian Sheng, Rui Guo, and Zheng Bao, *Senior Member, IEEE*

***Abstract*—Compressive sensing (CS) theory indicates that the optimal reconstruction of an unknown sparse signal can be achieved from limited noisy measurements by solving a sparsity-driven optimization problem. For inverse synthetic aperture radar (ISAR) imagery, the scattering field of the target is usually composed of only a limited number of strong scattering centers, representing strong spatial sparsity. This paper derives a new autofocus algorithm to exploit the sparse apertures (SAs) data for ISAR imagery. A sparsity-driven optimization based on Bayesian compressive sensing (BCS) is developed. In addition, we also propose an approach to determine the sparsity coefficient in the optimization by using constant-false-alarm-rate (CFAR) detection. Solving the sparsity-driven optimization with a modified Quasi-Newton algorithm, the phase error is corrected by combining a two-step phase correction approach, and well-focused image with effective noise suppression is obtained from SA data. Real data experiments show the validity of the proposed method.**

***Index Terms*—Bayesian compressive sensing (BCS), compressive sensing (CS), inverse synthetic aperture radar (ISAR), sparse aperture (SA).**

I. Introduction

DUE TO the superiorities over other remote sensing tools, such as high probability of target identification, robust performance under all-weather circumstances, and very long operating distance, inverse synthetic aperture radar (ISAR) is widely applied in many civilian and military fields [1], [2]. To realize these applications, the two-dimensional (2-D) high resolution is usually required to characterize target features in detail. In general, high down-range resolution depends on the system bandwidth. To mitigate this dependence, stepped frequency waveforms (SFWs) [3] are employed. High cross-range resolution is obtained by exploiting the multiple diversities of radar-viewing angles to the target, and then Doppler analysis can resolve scattering centers into different Doppler bins. The cross-range resolution depends on both the available CPI and intrinsic motion characteristics of the target. As is known, achieving high cross-range resolution usually requires a long CPI. However, in the situation of multitargets, long observation for a single target imaging is no longer acceptable in a modern radar system, attributed to its multiple functions, such as searching, locating, and tracking multiple targets simultaneously. Since targets may locate in different channels and beams as well as with different velocity vectors, radar system has to switch among different line-of-sight (LOS) angles to capture them. As a result, observation interval is assigned evenly to each target, resulting in sparse apertures (SAs) and gaps in the collected data. SAs would be also introduced in synthetic aperture radar (SAR) imaging with multiply angular diversities [4], [5], where a target is illuminated by several sensors from different angles independently and each sensor collects only a small angular region composing a sparse aperture. In SA-ISAR imaging, if the motion error is eliminated, a simple way to achieve image would be to apply Fourier transform with the missing data set to zero, bringing serious grating lobes in the image.

To reduce the discontinuous aperture effects on ISAR imagery, many novel approaches are ready to use. These approaches can be sorted into three groups: 1) CLEAN techniques [6]–[8] treat image formation from SA data as a deconvolution procedure. They estimate and subtract the main lobes of the strong scattering centers iteratively until reach a convergence. CLEAN techniques are usually efficient but sensitive to noise. 2) A number of modern spectral estimate approaches can cope with SA data effectively. They estimate the complex-valued amplitude and position of strong scatterers from gapped data based on interpolation of the missing data under certain constraints. The gapped-data amplitude and phase estimation (GAPES) [4], [9] and its extensions [10], [11] are representative approaches of this group. They can handle quite general SA patterns and perform well under some noisy circumstances. 3) Interpolation and extrapolation algorithms can be also solve the data missing problem in some situations. By fitting the available data into linear predication models, the missed data can be interpolated or extrapolated from the observed data. These methods also apply some modern spectral estimation techniques to obtain the coefficients of the prediction model. See some detailed approaches in [12]–[16]. The conventional approaches usually perform well in coping with SA data in some situations. However, they are more or less sensitive to additive noise and usually take nominal model error into consideration, especially evitable phase errors

Manuscript received January 03, 2011; revised June 16, 2011; accepted July 20, 2011. Date of publication October 21, 2011; date of current version February 03, 2012. This work was supported by the "973" Program of China under Grant 2010CB731903. The work of Z.-J. Qiao was supported by the U. S. Army Research Office under Grant No. W911NF-08-1-0511 and the Texas Norman Hackerman Advanced Research Program under Grant No. 003599-0001-2009.

L. Zhang, M.-D. Xing, J.-L. Sheng, R. Guo, and Z. Bao are with the National Key Laboratory of Radar Signal Processing, Xidian University, Xi'an 710071, China (e-mail: zhanglei_0330@126.com).

Z.-J. Qiao is with the Department of Mathematics, University of Texas–Pan American, Edinburg, TX 78539-2999 USA.

Color versions of one or more of the figures in this paper are available online at http://ieeexplore.ieee.org.

Digital Object Identifier 10.1109/TAP.2011.2173130

induced by undesired target motion. It should be emphasized that due to the discontinuities between subapertures, current approaches [17]–[21] are not satisfactory to be directly applied for phase adjustment. As the complex phase errors and noise are inevitable, conventional methods for the SA imaging encounter inherent limitations in real applications. Therefore, the error correction should be accounted in dealing with SA imaging to a large extent. Another significant factor, the signal-to-noise ratio (SNR) gain of the formatted image, also plays an important role in SA imagery. In ISAR imaging, radar signal is usually contaminated by strong noise, which is usually overcome by the coherent accumulation processing, providing a high SNR in the final image. It is well known that the SNR gain is proportional to the amount of signal accumulated. In SA-ISAR imaging, due to a large portion of data missed, the negative effect of noise would degrade the performance of current approaches to generate image with high SNR. Notably, the negative effects from both motion error and strong noise should be accounted seriously in SA-ISAR imaging.

The ISAR image demonstrates the distribution of strong scattering centers of the target's scattering field in the range-Doppler (RD) plane. The dominant scattering centers take only a fraction of the whole bins in the plane. In this sense, ISAR image represents strong spatial sparsity in the RD domain. Exploiting such sparsity is meaningful to achieve improved performance, such as super-resolution [22], feature enhancement [23], SAR imaging with model error correction [24], and simplicity of data acquirement [25]. More importantly, recent developing theory of the compressive sensing (CS) tells us that an unknown sparse signal is able to be exactly recovered from a very limited number of measurements with high probability by exploiting the sparsity of signal. This is implemented by solving a l_1-norm optimization problem [26]–[28]. In other words, the ill-posed problem, recovering high-dimensional signal from low-dimensional observations, could be solved by exploiting sparsity of the objective signal.

Following this idea, in this paper, we propose a novel algorithm for SA-ISAR imaging. In this algorithm, we focus on image formation from SA data and correction of the phase errors induced by translational motion. The SA-ISAR imaging and model error correction are converted into a problem of solving a sparsity-driven optimization problem corresponding to the maximum *a posteriori* (MAP) estimate in Bayesian compressive sensing (BCS) [29]. The sparsity-driven optimization is based on the assumption that the additive noise is subject to a zero-mean Gaussian distribution with unknown variance σ^2 and the signal components corresponding to the dominant scattering centers follow a Laplace distribution with coefficient γ independently. In the sparsity-driven optimization, the sparsity coefficient is directly related to σ^2 and γ. In order to precisely estimate the statistic parameters from SA data, we utilize the constant-false-alarm-rate (CFAR) detector to discriminate signal from noise in the subaperture images approximately. Using the pure noise and target components, both σ^2 and γ can be obtained via maximum likelihood (ML). In the SA-ISAR imaging algorithm, the phase adjustment is indispensably required as model error correction, and conventional CS solvers

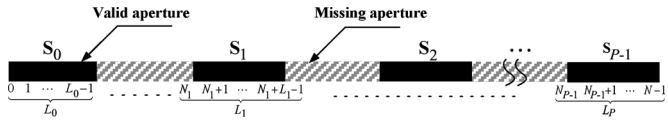

Fig. 1. SA geometry.

are not directly available herein. Therefore, we apply a modified Quasi-Newton algorithm for image formation jointed with phase adjustment, which is implemented in an iterative manner. A two-step phase adjustment is developed for coarse correction of motion error, which can reduce the phase error in a small level. In order to improve the efficiency of the solver, fast Fourier transform and conjugate gradient algorithm can be applied in its implementation. Real data experiments show that the sparsity-driven algorithm is capable of overcoming the grating lobes and yielding ISAR image with high SNR, even when the observations are very limited.

This paper is organized as follows. In Section II, we introduce the SA-ISAR imaging algorithm and the statistic estimation of σ^2 and γ. In Section III, the Quasi-Newton solver is presented in detail, together with a two-step phase adjustment for acceleration of the solver. In Section IV, we present results of real data experiments to validate the proposed method, and we give some conclusions in last section.

II. Sparsity-Driven Optimization for SA-ISAR Imaging

A. Signal Model for SA-ISAR Imaging

Considering that an ISAR system observes multiple targets simultaneously, radar illumination has to switch from one target to another evenly, resulting in sparse apertures for each target. At first, conventional range compression and range alignment are applied to the SA data with some current approaches [30]–[33], which are identical to those in the conventional ISAR imagery. The range-compressed and aligned signal is denoted by $\mathbf{S}$. Without loss of generality, we assume that there are P subapertures for a target consisting of a long sparse aperture. Fig. 1 shows the geometry of the sparse aperture. The full aperture should contain N pulses with index from 0 to $N-1$, and each pulse composes M range bins. Suppose that the pth subaperture consists of L_p pulses (whose index is from N_p to N_p+L_p-1). The range-compressed data set corresponding to the pth subaperture is given by (1), shown at the bottom of the next page. Then, the SA data matrix is

$$\mathbf{S}=\begin{bmatrix}\mathbf{S}_0\\ \vdots\\ \mathbf{S}_p\\ \vdots\\ \mathbf{S}_{\mathrm{P}-1}\end{bmatrix}. \tag{2}$$

We note that the SA data set has $\overline{N}=L_1+L_2+\cdots+L_P$ ($\overline{N}<N$) pulses. Clearly, in an ideal ISAR data collection, the returned signals can be regarded as a measuring patch of the two-dimensional Fourier transform of the target scattering field corresponding to some aspect angles. Due to the maneuver, the phase errors from complex motion of the target should be

accounted in signal modeling. Then, the echoed signals with phase error are rewritten in the following form:

$$\mathbf{S} = \mathbf{EFA} + \boldsymbol{\varepsilon} \tag{3}$$

where $\mathbf{A} = [a_{nm}]$ is an $N \times M$ matrix and denotes the 2-D ISAR image, whose pixel values are corresponding to scattering center amplitudes. ε is the additive noise matrix with the same size as $\mathbf{S}$. $\mathbf{F}$ stands for a partial Fourier matrix in size $\overline{N} \times N$, whose construction is corresponding to the SA structure. It is given by

$$\mathbf{F} = \begin{bmatrix} \mathbf{F}_0 \\ \vdots \\ \mathbf{F}_p \\ \vdots \\ \mathbf{F}_{\mathrm{P}-1} \end{bmatrix} \tag{4}$$

where

$$\mathbf{F}_p = \begin{bmatrix} 1 & \omega^{N_p} & \cdots & \omega^{(N-1)N_p} \\ 1 & \omega^{N_p+1} & \cdots & \omega^{(N-1)(N_p+1)} \\ \vdots & \vdots & \ddots & \vdots \\ 1 & \omega^{N_p+L_p-1} & \cdots & \omega^{(N-1)(N_p+L_p-1)} \end{bmatrix}_{L_p \times N}$$
$$\omega = \exp\left[-j\frac{2\pi}{N}\right]. \tag{5}$$

$\mathbf{F}_p$ is the partial Fourier matrix in accordance with the pth subaperture. In our SA-ISAR imaging, the structure of the sparse aperture of a certain target is assumed to be obtained. In other words, we can construct the exact partial Fourier matrix of $\mathbf{F}$ in advance. $\mathbf{E}$ is an $\overline{N} \times \overline{N}$ matrix and represents the phase errors from pulse to pulse

$$\mathbf{E} = \mathrm{diag}[\boldsymbol{e}] \tag{6}$$

where

$$\boldsymbol{e} = \begin{bmatrix} \boldsymbol{e}_0 \\ \vdots \\ \boldsymbol{e}_p \\ \vdots \\ \boldsymbol{e}_{\mathrm{P}-1} \end{bmatrix} \tag{7}$$

and $e_p = [\exp[j \cdot \phi(N_{p-1})], \cdots, \exp[j \cdot \phi(N_{p-1} + L_{p-1} - 1)]]^T$ denotes the phase error vector corresponding to the pth subaperture.

B. SA-ISAR Imaging via Exploiting Sparsity

Generally, the components of $\boldsymbol{\varepsilon}$ are approximated as a zero-mean complex Gaussian noise, namely, its imaginary and real parts (denoted by $\boldsymbol{\varepsilon_r}$ and $\boldsymbol{\varepsilon_i}$, respectively) independently follow Gaussian distributions with unknown variance σ^2. As a result, its probability density function is given by

$$\begin{aligned} \boldsymbol{P}(\boldsymbol{\varepsilon}|\sigma^2) &= (2\pi\sigma^2)^{-\frac{\bar{N}\cdot M}{2}} \exp\left(-\frac{1}{2\sigma^2}\|\boldsymbol{\varepsilon}_r\|_2^2\right) \\ &\quad \times (2\pi\sigma^2)^{-\frac{\bar{N}\cdot M}{2}} \exp\left(-\frac{1}{2\sigma^2}\|\boldsymbol{\varepsilon}_i\|_2^2\right) \\ &= (2\pi\sigma^2)^{-\bar{N}\cdot M} \exp\left(-\frac{1}{2\sigma^2}\|\boldsymbol{\varepsilon}\|_2^2\right). \end{aligned} \tag{8}$$

The $\|\mathbf{Q}\|_2^2$ notation for a matrix $\mathbf{Q}$ denotes $\|\mathbf{Q}\|_2^2 = \sum_{n,m}[\mathbf{Q}(n,m)]^2$. Therefore, we have the Gaussian likelihood model of the observation, which is

$$\boldsymbol{P}(\mathbf{S}|\mathbf{A},\sigma^2) = (2\pi\sigma^2)^{-\bar{N}\cdot M} \exp\left(-\frac{1}{2\sigma^2}\|\mathbf{S} - \mathbf{EFA}\|_2^2\right). \tag{9}$$

ISAR imagery demonstrates the distribution and amplitudes of limited dominant centers of the target, which usually represents strong sparsity. According to Bayesian compressive sensing [29], the sparsity can be formulized by placing a sparseness-promoting prior on $\mathbf{A}$. Herein, this sparseness prior is represented by the Laplace density function.

$$\boldsymbol{P}(\mathbf{A}\|\gamma) = \left(\frac{\gamma}{2}\right)^{N\cdot M} \exp\left(-\gamma\|\mathbf{A}\|_1\right) \tag{10}$$

where $\|\mathbf{A}\|_1 = \sum_{n=0}^{N-1}\sum_{m=0}^{M-1}|\mathbf{A}(n,m)|$. Then, SA-ISAR imagery is shifted into a classical problem to estimate $\mathbf{A}$ from noisy observation $\mathbf{S}$. For this purpose, the MAP estimator is used, which is given by

$$\hat{\mathbf{A}}(\mathbf{S}) = \arg\max_{\mathbf{A}\in\mathbf{C}_{N\times M}} [\boldsymbol{P}(\mathbf{A}|\mathbf{S})]. \tag{11}$$

Using the Bayes rule, one gets

$$\hat{\mathbf{A}}(\mathbf{S}) = \arg\max_{\mathbf{A}\in\mathbf{C}_{N\times M}} \left[\boldsymbol{P}(\mathbf{S}|\mathbf{A},\sigma^2)\cdot\boldsymbol{P}(\mathbf{A}|\gamma)\right]. \tag{12}$$

Clearly, (11) is also equivalent to

$$\hat{\mathbf{A}}(\mathbf{S}) = \arg\max_{\mathbf{A}\in\mathbf{C}_{N\times M}} \left\{\log\left[\boldsymbol{P}(\mathbf{S}|\mathbf{A},\sigma^2)\right] + \log\left[\boldsymbol{P}(\mathbf{A}|\gamma)\right]\right\}. \tag{13}$$

$$\mathbf{S}_p = \begin{bmatrix} s(N_p,0) & s(N_p,1) & \cdots & s(N_p,M-1) \\ s(N_p+1,0) & s(N_p+1,1) & \cdots & s(N_p+1,M-1) \\ \vdots & \vdots & \vdots & \vdots \\ s(N_p+L_p-1,0) & s(N_p+L_p-1,1) & \cdots & s(N_p+L_p-1,M-1) \end{bmatrix}_{L_p\times M}. \tag{1}$$

Substituting (9) and (10) into (13), the MAP estimator becomes

$$\hat{\mathbf{A}}(\mathbf{S}) = \arg \max_{\mathbf{A}\in\mathbf{C}_{N\times M}} \left\{ -\frac{1}{2\sigma^2}\|\mathbf{S}-\mathbf{EFA}\|_2^2 - \gamma\|\mathbf{A}\|_1 \right\} = \arg \min_{\mathbf{A}\in\mathbf{C}_{N\times M}} \left\{ \|\mathbf{S}-\mathbf{EFA}\|_2^2 + \mu\|\mathbf{A}\|_1 \right\} \quad (14)$$

where $\mu = 2\sigma^2\gamma$ is the sparsity coefficient, which is directly related to the unknown statistic of noise and target signal. The optimization problem consists of two different terms: The l_2-norm preserves the data fidelity of the solution, and the l_1-norm imposes it to be sparse. Clearly, based on the assumption of Gaussian and Laplace distributions, the MAP estimator of SA-ISAR imagery is corresponding to an l_1-norm regularization optimization problem, which is often called basis pursuit denoising (BPDN) [34]. BPDN is often concerned as a well-suited estimator of sparse signal from limited measurements. It also can overcome the noise interference effectively. Clearly, different from conventional SA imaging algorithms, the MAP estimator aims at reconstructing denoised image with full resolution. Compared to the point-enhanced algorithm [23], the sparsity-weighting coefficient in the optimization (14) has an analytic expression in mathematics: It is directly associated with the statistics of noise and target in a Bayesian sense. However, besides the unknown phase error, a significant problem of solving (14) for SA imaging lies in the determination of μ. Only when a precise value of the sparsity coefficient is given can we reconstruct an optimal ISAR image from limited noisy SA data. Nevertheless, if μ is set too large, weak scatterers together with noise will be rejected in the reconstruction of image, and only the dominant scattering centers are preserved. If μ is overly small, then a significant part of noise elements may be left in the image, degrading the image quality. Derived from the MAP estimation, the sparsity coefficient μ is deterministic if we have the prior information about σ^2 and γ. In Section II-C, we propose an approach to estimate them from subaperture images.

C. Estimation of σ^2 and γ

The estimation of σ^2 and γ from SA data can be used as prior information. Estimation of the noise variance is available since Gaussian noise usually distributes evenly, and there exists a large number of cells containing only noise in the RD plane. Given enough noise samples by those pure noise bins, we can estimate σ^2 with high accuracy. Meanwhile, γ of the Laplace distribution placed on $\mathbf{A}$ can be estimated from the signal bins. Herein, the estimation of the statistical parameters of noise and ISAR image contains the following two steps.

Step 1) SA images are generated by conventional ISAR imaging procedure. Noise variance is estimated by using pure noise samples.

Step 2) Scattering centers of target are determined by CFAR detector in the SA images. Meanwhile, the noise bins are set to be zero, and maximum likelihood estimation of γ is performed by using the denoised SA images.

In Step 1, we first perform conventional imaging processing to each SA data, including translational motion removal and azimuth compression. As conventional range alignment and phase adjustment are suitable to correction of translational motion within the subaperture data, each self-organized subaperture is ready to generate a low-resolution image with the range-Doppler algorithm. In the SA image, the target is placed round the zero Doppler as the Doppler shift is removed in the translational motion compensation, which indicates that the cells corresponding to high Doppler frequency contain noise only. Herein, we use these bins as noise samples. As we assume the noise follows zero-mean Gaussian distribution, the ML estimator of σ^2 is the variance of all real and imaginary parts of noise samples (defined as $\hat{\sigma}^2$). Because there are P SA images, one usually has enough noise samples, and $\hat{\sigma}^2$ trends to the exact value.

In Step 2, the first is the detection process to separate scattering centers from noise in the SA images. Due to high SNR gained from the 2-D coherent integration, strong scattering centers are distinctive from noise in the SA images. Herein, discriminating target bins from noise in the SA images corresponds to a problem of distributed target detection under the background of Gaussian noise. Utilizing the noise samples from Step 1, a CFAR detector for target scatters detection is straightforward. Then, we can use these noise samples to develop a CFAR detector for strong scattering centers. For an extensive study of CFAR detector, [35] and [36] can be consulted. Then, bins with amplitudes larger than the CFAR threshold are determined as target components, and the rest are regarded as noise and set to be zero. After the above denoising processing, the pth SA image is defined as $\tilde{\mathbf{A}}_p$. The ML estimator of γ is found by maximizing

$$\boldsymbol{P}(\tilde{\mathbf{A}}_p|\gamma) = \left(\frac{\gamma}{2}\right)^{L_p\cdot M} \cdot \exp\left(-\gamma\|\tilde{\mathbf{A}}_p\|_1\right) = \prod_{l=0,m=0}^{L_p-1,M-1} \left(\frac{\gamma}{2}\right) \exp\left(-\gamma\left\|\tilde{\mathbf{A}}_p(l,m)\right\|_1\right). \quad (15)$$

It is equivalent to maximizing $\log[P(\tilde{A}_p|\gamma)]$. Differentiating with respect to γ produces

$$\frac{\partial \log\left[\boldsymbol{P}(\tilde{\mathbf{A}}_p|\gamma)\right]}{\partial\gamma} = \frac{L_p\cdot M}{\gamma} - \sum_{l=0}^{L_p-1}\sum_{m=0}^{M-1}\left|\tilde{\mathbf{A}}_p(l,m)\right|. \quad (16)$$

Setting (24) equal to zero yields the ML estimator of the pth SA image

$$\hat{\gamma}_p = \frac{L_p\cdot M}{\sum_{l=0}^{L_p-1}\sum_{m=0}^{M-1}\left|\tilde{\mathbf{A}}_p(l,m)\right|}. \quad (17)$$

Clearly, the ML estimator of $\hat{\gamma}_p$ is the the reciprocal of the mean of all pixel values. Finally, we average the estimates of all SA images to obtain the estimation of γ, which gives

$$\hat{\gamma} = \frac{1}{P}\cdot\sum_{p=0}^{P-1}\hat{\gamma}_p. \quad (18)$$

By using $\hat{\sigma}^2$ and $\hat{\gamma}$, the sparsity coefficient is obtained easily, which is given by $\hat{\mu} = 2\hat{\sigma}^2\hat{\gamma}$. For clarity, we give conceptual flowchart by using the Yak-42 data in Fig. 2.

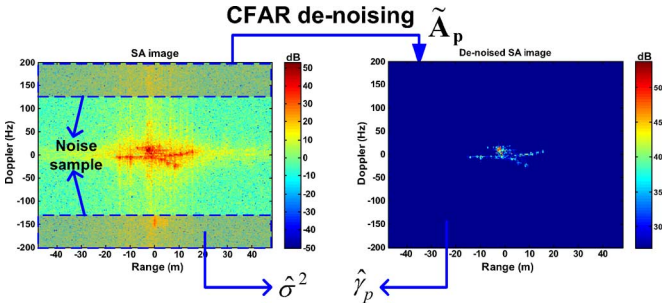

Fig. 2. Statistic estimation from SA image.

Generally, as we use the target samples from subaperture images to estimate the statistics of the full aperture image, some estimation error is inevitable. However, in real applications, we find $\hat{\mu}$ performs well in different situations, although it usually trends to be excessively large. A drawback of the estimator for $\hat{\gamma}$ lies in the need of a considerable amount of pulses in a subaperture, which may limit its usage in some special cases, such as very short SA and random sampled SA patterns. In these cases, the high SNR gain by the 2-D coherent integration may not be achievable, and thus signal components are submerged by the strong noise, which will be studied in our future work.

III. Modified Quasi-Newton Solver for SA-ISAR Imaging

A. Modified Quasi-Newton Solver for Image Formation and Phase Adjustment

Clearly, formation of the full-aperture resolution image by SA data is an ill-posed problem. Due to the data missing among the subapertures, the pulse amount $(\overline{N})$ is much less than that of Doppler bins (N) of the high-resolution image. According to the theory of the compressive sensing, SA-ISAR imagery is possible by solving the l_1-norm optimization problem in (13), and it is also widely accepted that the problem is equivalent to the l_1-norm constraint optimization in compressive sensing [37], for which many efficient solvers are available [38]–[40]. Nevertheless, these methods are not directly applicable to (13) due to the phase errors $\mathbf{E}$ induced by unexpected target motion. In this section, we present a modified Quasi-Newton solver for ISAR imaging from SA data, joint with correction of phase error from translational motion. At first, in order to overcome the nondifferentiability of the l_1-norm around the origin in (13), a useful approximation [23], [41], [42] is employed by

$$\|\mathbf{A}\|_1 \approx \sum_{n=0}^{N-1}\sum_{m=0}^{M-1}\left(|a_{mn}|^2+\tau\right)^{1/2} \tag{19}$$

where $|\cdot|$ stands for the modulus operator, and τ is a small nonnegative parameter. Clearly, to ensure the approximation as rigid as possible, τ should be set small. Thus, the MAP estimator of the image in (13) can be reformatted as

$$\hat{\mathbf{A}}(\mathbf{S}) = \arg\min_{\mathbf{A}\in\mathbf{C}_{N\times M}}\left\{\|\mathbf{S}-\mathbf{EFA}\|_2^2 + \mu\sum_{n=0}^{N-1}\sum_{m=0}^{M-1}\left(|a_{nm}|^2+\tau\right)^{1/2}\right\}. \tag{20}$$

This problem is a 2-D optimization. To make it is easy to solve. We first convert it to one-dimensional (1-D) problems. The optimization (20) can be rewritten as

$$\hat{\mathbf{A}}(\mathbf{S}) = \arg\min_{\mathbf{A}\in\mathbf{C}_{N\times M}}\left\{\sum_{m=0}^{M-1}\left[\|\mathbf{s}_m-\mathbf{EFa}_m\|_2^2 + \mu\sum_{n=0}^{N-1}\left(|a_{nm}|^2+\tau\right)^{1/2}\right]\right\} \tag{21}$$

where $\mathbf{s}_m = \mathbf{S}(:,m)$ and $\mathbf{a}_m = \mathbf{A}(:,m)$ denote the SA signal of the mth range cell and the mth column of the high resolution 2-D image, respectively. Due to the independence between the range cells, solving the 2-D optimization (20) is equivalent to figure out the following 1-D optimization for all range cells separately. For the reconstruction of the mth column of $\mathbf{A}$, we have the following optimization:

$$\hat{\mathbf{a}}_m(\mathbf{S}) = \arg\min_{\mathbf{a}_m\in\mathbf{C}_{N\times 1}}\|\mathbf{s}_m-\mathbf{EFa}_m\|_2^2+\mu\sum_{n=0}^{N-1}\left(|a_{nm}|^2+\tau\right)^{1/2}. \tag{22}$$

Hence, the conjugate gradient function of $f(\mathbf{a}_m) = \|\mathbf{s}_m - \mathbf{EFa}_m\|_2^2 + \mu\sum_{n=0}^{N-1}(|a_{nm}|^2+\tau)^{1/2}$ with respect to a_m is calculated through

$$\begin{aligned}\nabla_{\mathbf{a}_m^*} f(\mathbf{a}_m) &= 2\mathbf{F}^H\mathbf{E}^H\mathbf{EFa}_m + \mu\mathbf{W}(\mathbf{a}_m)\cdot\mathbf{a}_m - \mathbf{F}^H\mathbf{E}^H\mathbf{s}_m \\ &= \mathbf{H}(\mathbf{a}_m)\cdot\mathbf{a}_m - \mathbf{F}^H\mathbf{E}^H\mathbf{s}_m\end{aligned} \tag{23}$$

where the Hessian matrix is approximately given by

$$\begin{aligned}\mathbf{H}(\mathbf{a}_m) &= 2\mathbf{F}^H\mathbf{E}^H\mathbf{EF} + \mu\mathbf{W}(\mathbf{a}_m) \\ &= 2\mathbf{F}^H\mathbf{F} + \mu\mathbf{W}(\mathbf{a}_m)\end{aligned} \tag{24}$$

and

$$\mathbf{W}(\mathbf{a}_m) = \operatorname{diag}\left[1\Big/\left(|a_{0m}|^2+\tau\right)^{1/2}, 1\Big/\left(|a_{1m}|^2+\tau\right)^{1/2}, \cdots, 1\Big/\left(|a_{(N-1)m}|^2+\tau\right)^{1/2}\right]. \tag{25}$$

Because the Hessian approximation relies on the objective $\mathbf{a}_m$, an iterative solver to (22) is presented through the following formula:

$$\hat{\mathbf{a}}_m^{(g+1)} = \left[\mathbf{H}\left(\hat{\mathbf{a}}_m^{(g)}\right)\right]^{-1}\mathbf{F}^H\left[\hat{\mathbf{E}}^{(g)}\right]^H\mathbf{s}_m \tag{26}$$

where $\hat{\mathbf{a}}_m^{(g)}$ and $\hat{\mathbf{E}}^{(g)}$ are the estimators of $\mathbf{A}(:,m)$ and $\mathbf{E}$ in the gth iteration, respectively. To accelerate the update, conjugate gradient algorithm (CGA) can be applied to avoid the matrix inverse calculation. In the case of no prior information about the phase error, starting from the initial value $\hat{\varphi}(n) = 0$ and $\hat{\mathbf{A}} = \mathbf{F}^H\mathbf{S}$, then we have the estimator of the phase error $\varphi(n)$ in the $(g+1)$th iteration (denoted by $\hat{\varphi}^{(g+1)}(n)$)

$$\hat{\varphi}^{(g+1)}(n) = \hat{\varphi}^{(g)}(n) + \Delta\hat{\varphi}^{(g+1)}(n). \tag{27}$$

Here, the updating exponential term of the phase error is given by

$$\exp\left[j\cdot\Delta\hat{\varphi}^{(g+1)}(n)\right]=\frac{\left[\hat{\mathbf{S}}^{(g+1)}(:,n)\right]^{H}\cdot\mathbf{S}(:,n)}{\left|\left[\hat{\mathbf{S}}^{(g+1)}(:,n)\right]^{H}\cdot\mathbf{S}(:,n)\right|} \quad (28)$$

and

$$\hat{\mathbf{S}}^{(g+1)}=\hat{\mathbf{E}}^{(g)}\mathbf{F}\hat{\mathbf{A}}^{(g+1)}. \quad (29)$$

In the sparstiy-driven SA-ISAR algorithm, we consider the phase error among the pulses. The phase error is corrected during the image formation in an iterative manner. It should be noted that there are no constraints on concrete form of phase errors in the solver, and even when the phase errors vary randomly from pulse to pulse, it is capable of achieving high quality SA-ISAR images. The computational load of the Quasi-Newton solver is a significant to its real applications. We note that major computational load of in each update sources from the matrix inversion calculation of $\mathbf{H}(\hat{\mathbf{a}}_m^{(g)})$ in (24), which is implemented by CGA. However, due to the iterative property of CGA, its efficiency may be slow as one need to perform the calculation of the linear equation $\mathbf{H}(\hat{\mathbf{a}}_m^{(g)})\hat{\mathbf{a}}_m^{(g+1)}=\mathbf{F}^H[\hat{\mathbf{E}}^{(g)}]^H\mathbf{s}_m$ many times. Its major computational load lies in the multiplication of $\mathbf{F}^H\mathbf{F}\hat{\mathbf{a}}_m^{(g+1)}$ in $\mathbf{H}(\hat{\mathbf{a}}_m^{(g)})\hat{\mathbf{a}}_m^{(g+1)}$. As the term $\mathbf{F}^H\mathbf{F}$ corresponds to the partial Fourier matrix, allowing us to use fast Fourier transform (FFT) to implement $\mathbf{F}^H\mathbf{F}\mathbf{a}$ ($\mathbf{a}$ denotes an N-dimensional vector) efficiently: We perform the inverse FFT to $\mathbf{a}$ and obtain $\mathbf{a}_t$, then set the components corresponding to the vacant apertures to zero and followed FFT. For simplicity, only the multiple operations are accounted. Therefore, taking only the multiple operations into account, $\mathbf{F}^H\mathbf{F}\mathbf{a}$ can be implemented with only $N\log_2 N$ flops corresponding to two FFTs. For the number of the CGA iterations to solve (26) being T_{CGA} case, the computational cost of CGA is about $T_{\mathrm{CGA}}N\log_2 N$ flops. Assuming there are T_{QN} times of iterations in the Quasi-Newton solver, the computational cost by using FFT is $T_{\mathrm{QN}}T_{\mathrm{CGA}}N\log_2 N$ flops approximately.

B. Efficiency Improvement by Combining Conventional Phase Adjustment

The major problem of the Quasi-Newton solver in dealing with severe phase errors lies in its low efficiency. From the viewpoint of optimization, appropriate initialization of $\mathbf{A}$ and $\mathbf{E}$ is essential to improve the efficiency and accuracy of the Quasi-Newton solver. Precise initialization can dramatically reduce the iteration number to achieve a satisfactory solution to the optimization problem. However, precise prior information of $\mathbf{A}$ and $\mathbf{E}$ is usually not achievable. Herein, the initialization of $\mathbf{A}$ is achieved by setting the vacant apertures to zero and applying FFT. Preprocessing of motion compensation should be carried out to suppress the phase errors as much as possible, which would put much less burden on the Quasi-Newton solver and enhance its convergence with much less iterations. Due to the data discontinuity, phase adjustment for the SA data is quite different from the conventional ISAR scenarios. Herein, we propose two-step preprocessing for phase error reduction.

In the first step, we utilize the Doppler tracking technique. Without assumption of even and full aperture, the Doppler tracking technique still works by multiple prominent points processing (PPP) [2]. The basic idea of the multiple PPP algorithm is to track the phase history of one or more isolated point-scatters in aligned range profiles in order to extract phase errors. The main challenge in applying the multiple PPP algorithm is the selection of the point-like prominent scatterers, which should be well isolated in their respective range cells. It is easily found that this method performs well in artificial targets with dominant scatters, for instance, airplanes, missiles and ships, etc. The PPP procedure includes three steps: 1) searching for one or several reference range cells by using some criteria like minimum variance; 2) taking conjugate phase at the reference range cells and combining them together by weighting; and 3) making phase correction for all range cells by the conjugate phase. However, in the presence of strong noise or absence of prominent points, the precision of the Doppler tracking may degrade. Therefore, Doppler tracking by the multiple PPP serves as a coarse step.

In the second step, we perform conventional phase adjustment to each subaperture to suppress phase errors within subaperture effectively. Note that each subaperture has a self-organized structure where the pulses are distributed continuously and evenly. Therefore, we can apply precise phase adjustment to eliminate the residual phase errors for each subaperture. Many phase adjustment algorithms could be applied to implement this step, such as the weighted least-squares phase estimation (WLSPE) [18] and the time-frequency transform-based auto-focusing [19]. This step can be regarded as a fine step for the phase error correction. Nevertheless, phase correction is performed on each subaperture independently, and thus phase errors within a subaperture can be eliminated to a nominal level. WLSPE is robust to noise, and as it directly extracts phase error rather than phase gradient, there is no significant additional linear phase in each SA data. In real application, we always apply it to implement the fine correction. However, residual phase errors still exist among different subapertures. By two-step preprocessing for phase adjustment, the majority of phase errors are removed, and only a fraction of them are left for the sparsity-driven algorithm, improving its efficiency dramatically. Considering the phase error difference within a subaperture is removed in the second step, for the pth subaperture, we have

$$\phi(N_{p-1})=\phi(N_{p-1}+1)=\cdots=\phi(N_{p-1}+L_{p-1}-1). \quad (30)$$

In the phase error estimations (27) and (28) of the sparsity-driven SA-ISAR imaging, we may reformat the update of phase error for the pth subaperture in a simpler way

$$\begin{aligned}\hat{\varphi}^{(g+1)}(N_{p-1})&=\hat{\varphi}^{(g+1)}(N_{p-1}+1)\cdots\\&=\hat{\varphi}^{(g+1)}(N_{p-1}+L_p-1)\\&=\hat{\varphi}^{(g)}(N_{p-1})+\Delta\hat{\varphi}^{(g+1)}(N_{p-1}).\end{aligned} \quad (31)$$

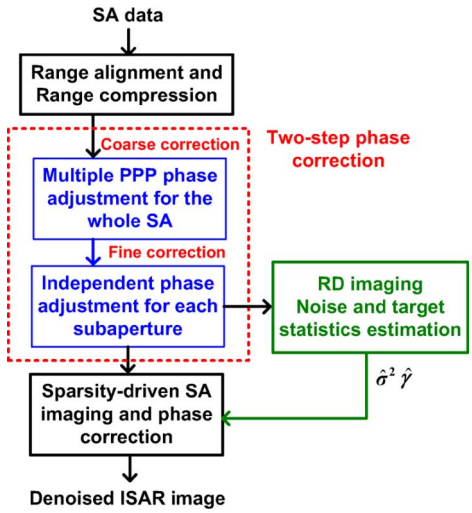

Fig. 3. Flowchart of the SA-ISAR imaging.

Here, the updating exponential term of the phase error is reformatted as

$$\exp\left[j\cdot\Delta\hat{\varphi}^{(g+1)}(N_{p-1}-1)\right]=\frac{\mathrm{sum}\left[\mathrm{conj}\left[\hat{\mathbf{S}}_p^{(g+1)}\right]\odot\mathbf{S}_p\right]}{\mathrm{sum}\left[\left|\mathrm{conj}\left[\hat{\mathbf{S}}_p^{(g+1)}\right]\odot\mathbf{S}_p\right|\right]} \tag{32}$$

and

$$\hat{\mathbf{S}}_p^{(g+1)}=\hat{\mathbf{E}}^{(g)}\mathbf{F}_p\hat{\mathbf{A}}^{(g+1)} \tag{33}$$

where $\mathrm{sum}[\cdot]$ denotes the operator to sum up all the matrix elements; $\mathrm{conj}[\cdot]$ is the conjugate operator, and $\odot$ represents Hadamard multiplication. The convergence for the iteration is straightforward. Let g increase, then we may repeat the iterative procedure in the optimization problem until we have

$$\frac{\left\|\hat{\mathbf{A}}^{(g+1)}-\hat{\mathbf{A}}^{(g)}\right\|_2^2}{\left\|\hat{\mathbf{A}}^{(g)}\right\|_2^2}<\rho \tag{34}$$

where the constant ρ is chosen as small as the predetermined threshold. Additionally, we can terminate the iteration, when g exceeds a predetermined number. Due to the two-step phase adjustment, the residual phase error is small. Therefore, an optimal solution can be obtained by the Quasi-Newton algorithm with only several iterations. For example, in the following experiments, only five iterations are used for the SA with a quarter of pulses missing. To make it clear, a flowchart for the SA-ISAR imaging is given in Fig. 3.

IV. Performance Analysis With Experiments

In this section, real ground-based measurements are used to generate synthetic data for carrying out a performance analysis of the SA-ISAR imaging by the sparsity-driven optimization. Accounting for the special cases of the ISAR imaging with noisy SA measurements, the performance analysis is carried out by considering two aspects: the phase error and the sparse aperture pattern. The experiments here are vital to validate the effectiveness of our approach.

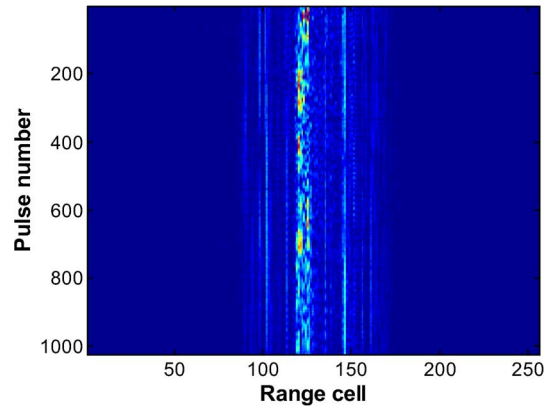

Fig. 4. Aligned range profiles.

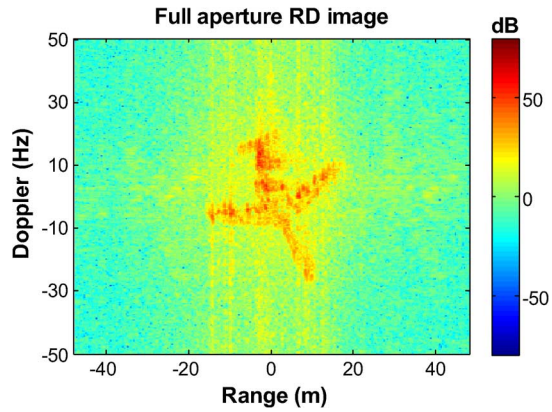

Fig. 5. RD image after auto-focusing.

A. Data Set and Experimental Conditions

In our algorithm for the SA-ISAR imaging, the sparsity of the target scattering field is exploited to overcome the model error and form a well-focused image. We believe that the inherent sparsity of a real ISAR target is difficult to be represented by simple simulated data. To make it convincing, we utilize the real measured ISAR data to perform different experiments. A data set of Yak-42 airplane is recorded by a C-band (5.52 GHz) ISAR experimental system. The system transmits 400-MHz linear modulated chirp signal with 25.6-μs pulse width, providing a range resolution of 0.375 m. The received signal is dechirped and I/Q sampled for range compression. We notice that since tracking errors are involved in the reference distances for the dechirping on receiving, random initial phase is introduced for each pulse. Range alignment and phase adjustment are required before we perform azimuth compression to the full-aperture data. The pulse repetition frequency is 400 Hz without undersampling. The data set consists of 1024 pulses. Conventional range alignment is applied to the data set eliminating the MTRC. The aligned profiles are shown in Fig. 4. From the aligned profiles, we know that several prominent scattering centers are available. For comparison, we apply the WLSPE to the data set and then generate the RD image shown in Fig. 5. The generated image is well focused, which can be used as a standard image for evaluating experimental results from sparse apertures. The estimated phase errors from a full

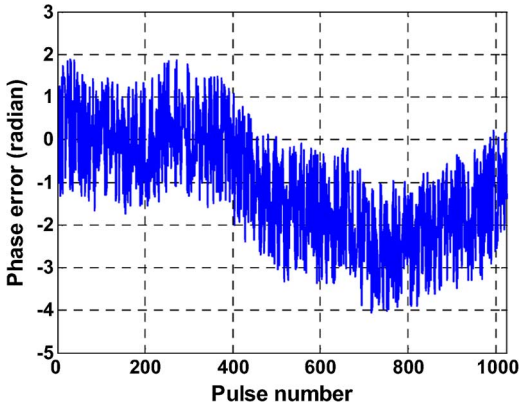

Fig. 6. Full aperture phase errors with WLSPE.

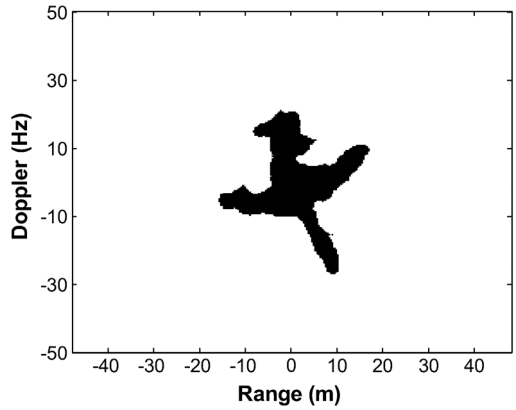

Fig. 7. Target region.

aperture are shown in Fig. 6, from which we note that due to the complex motion and dechirping on receiving, the phase errors are in a random pattern. In the following SA-ISAR imaging experiments, these phase errors are overcome by the two-step phase correction and the sparsity-driven imaging algorithm jointly. Phase error estimation in Fig. 6 is utilized as the criterion to evaluate the precision of the SA phase adjustment.

To provide a quantitative evaluation for the following SA-ISAR imaging experiment, we consider two metrics. The first evaluation metric could be the target-to-background ratio (TBR). By applying an adaptive threshold on the full-resolution image in Fig. 5 to separate the target and the background regions and then counting the target energy (within the target region) and noise energy of the reconstructed image, the TBR is given by

$$\mathrm{TBR} = 10 \cdot \log 10 \left(\frac{\sum_{(n,m)\in R_{\mathrm{T}}} \left| \hat{\mathbf{A}}(n,m) \right|^2}{\sum_{(n,m)\in R_{\mathrm{B}}} \left| \hat{\mathbf{A}}(n,m) \right|^2} \right) \tag{35}$$

where R_{T} and R_{B} are the predetermined target and background region shown in Fig. 7. It can also measure the target energy preservation with the help of the target region. Herein, we use the signal energy within the target region as the other metric, which is given by

$$\mathrm{SE} = 10 \cdot \log 10 \left(\sum_{(n,m)\in R_{\mathrm{T}}} \left| \hat{\mathbf{A}}(n,m) \right|^2 \right) \tag{36}$$

In the following SA imaging experiment, both TBR and SE are utilized as the quantitative metric to evaluate the SA image quality.

B. SA-ISAR Imagery Comparison With GAPES

In this section, we simulate the SA data of one target collected by a radar system observing multiple targets. In this scenario, the data amount corresponding to one target decreases along with the increase of the target amount. In the following experiment, we extract echoes from the complete aperture data set of Yak-42 plane as SA samples for simulation. The SAs with 512, 256, and 128 pulses are regarded as Case 1, 2, and 3 respectively. To test the robustness of the approach, we add complex-valued Gaussian noise into the SA data sets to generate different SNRs (20, 10, and 5 dB). Herein, the SNR is defined as the energy ratio between the original data set and the added noise. In our experiments, we consider that the pulse amount within a subaperture is 128. Collecting 128 pulses is achieved within a very short observation for a conventional ISAR system (0.32 s), which should not conflict with other radar activities including tracking and locating for multiple targets. In all experiments, the SA-ISAR imaging procedure in Fig. 3 is applied. The weights μ in the optimizations are estimated with the CFAR-based approach, and the CFAR is set to 10^{-4}. For the purpose of comparison, we also provide the ideal sparsity coefficients calculated by using the ideal γ ML-estimated from the image in Fig. 5 and the real noise variances under different SNRs. The estimated sparsity coefficients and the ideal ones are all listed in Table I. Clearly, there is some difference between the estimated and ideal sparsity coefficients; one can note that the difference within a single SA are very small. By using the estimated sparsity coefficients, optimizations under different SNRs and SA cases are developed.

TABLE I
ESTIMATED AND IDEAL γ IN SA1 PATTERN

	SNR=20dB	SNR=10dB	SNR=5dB
Case 1	46.2	446.8	1584.4
Case 2	44.6	454.2	1577.8
Case 3	47.4	473.0	1692.9
Ideal coefficient	46.5	465.1	1470.5

For all cases above, we first exploit the two-step phase adjustment to reduce the phase error. However, by comparing the results to those via WLSPE in Fig. 6, there still exist residual phase errors, as plotted in red in Fig. 8. Note that we only show the outcomes of Cases 1 and 2 since the results of Case 3 are identical to those in the first SA of the other two cases correspondingly. Although the residual phase errors are small within a single SA, among different SAs they vary in a large range almost one radian difference. The proposed sparsity-driven algorithm with (32) is expected to correct the rest phase difference

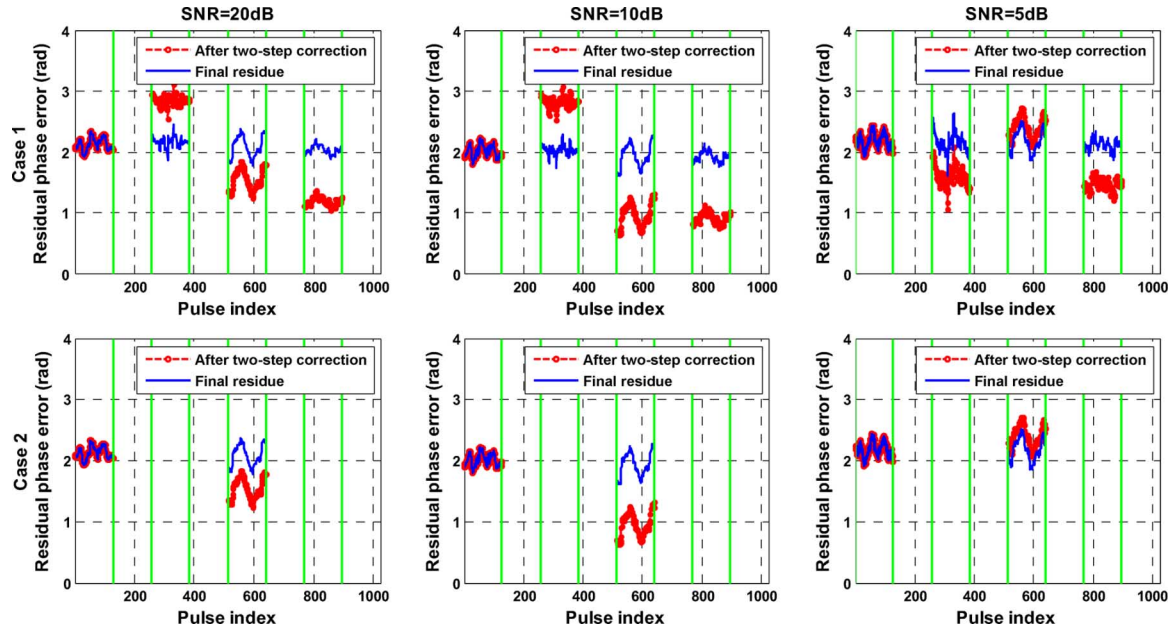

Fig. 8. Phase adjustment evaluation.

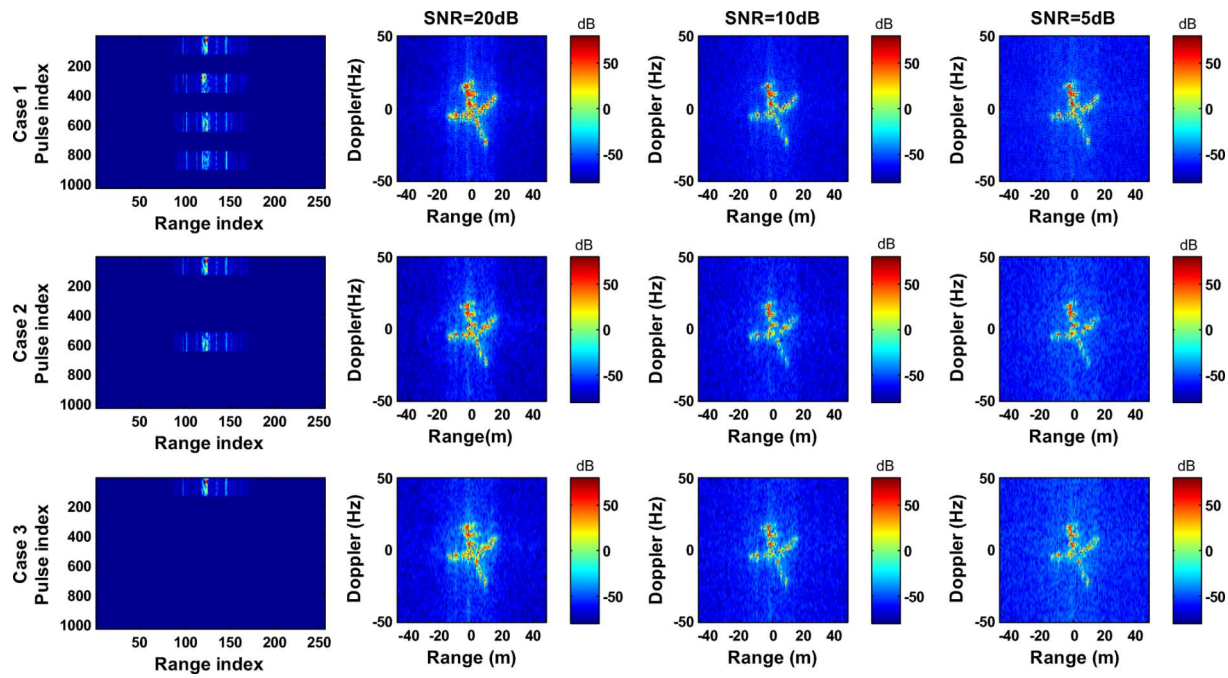

Fig. 9. Results with the proposed approach.

between SAs. The residual phase errors via sparsity-driven correction with 20 iterations are plotted in blue in Fig. 8. It is explicit to see that since the constant difference between different SAs is removed effectively via sparsity-driven correction, the residual phase errors are at the same level. Therefore, the phase difference becomes nominal which promises good performance of imaging.

Fig. 9 shows the SA imaging results by using the proposed approach under different SNRs. The first column of Fig. 9 gives the sparse aperture patterns with different SA numbers (4, 2, and 1). Different rows in Fig. 9 correspond to imaging results with different cases. The second, third, and right columns give the imaging results under $\mathrm{SNR} = 20$, 10, and 5 dB, respectively. One notes that, in all cases, well-focused images are achieved, which validates the effectiveness of our algorithm. For comparison, we also use the GAPES to process SA data under the same conditions. It should be emphasized that, as GAPES requires no phase error within the SA data, the phase error is precorrected before we extract SAs from original data in Fig. 6. The image results obtained by GAPES are given in Fig. 10. For both SA approaches, the decrease of measurements amount yields some noise increase in the reconstructed image, as we can see from Figs. 9 and 10. However, the sparsity-driven SA-ISAR imaging generally removes major noise producing image with

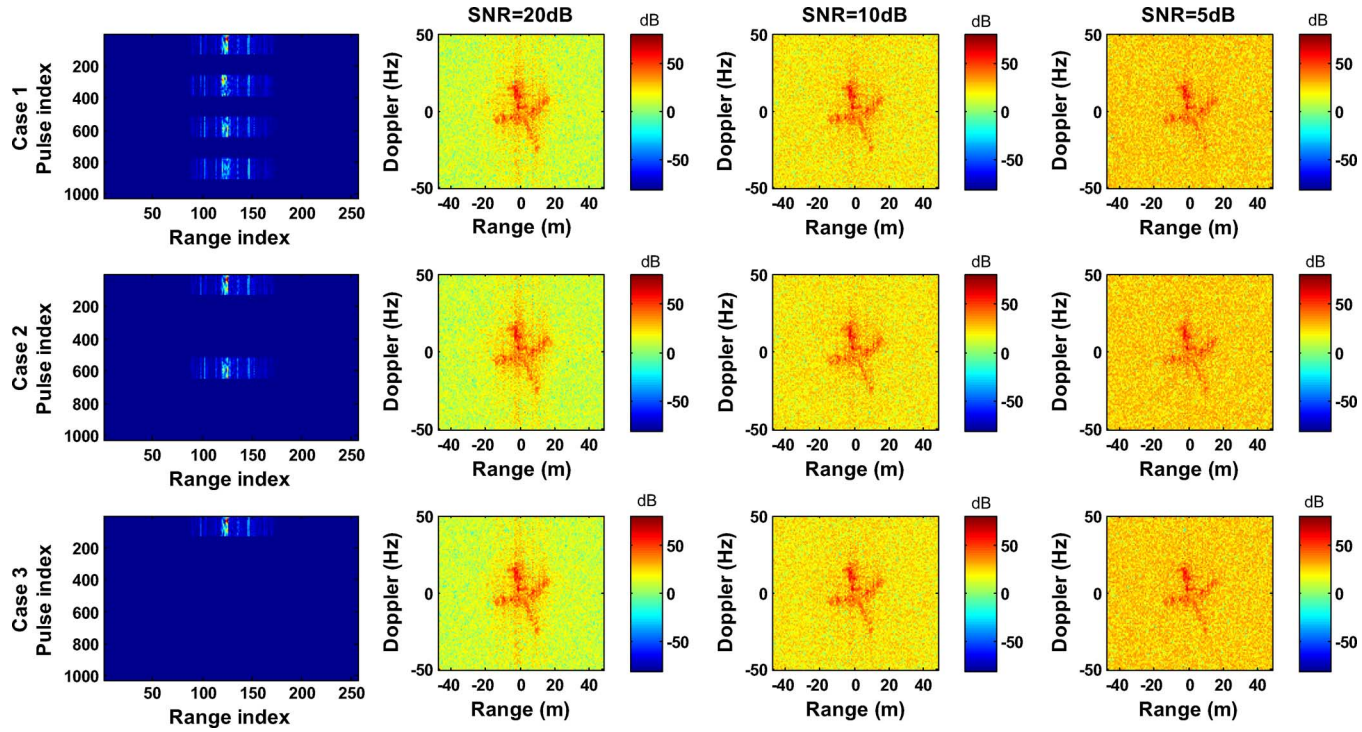

Fig. 10. Results with GAPES.

TABLE II
TBR OF IMAGES (dB)

	SNR=20dB	SNR=10dB	SNR=5dB
Proposal (case 1)	77.8	83.8	108.8
Proposal (case 2)	72.9	80.5	97.7
Proposal (case 3)	64.9	69.3	80.1
GAPES (case 1)	27.6	18.3	10.1
GAPES (case 2)	27.6	18.1	10.3
GAPES (case 3)	27.6	18.3	10.2

TABLE III
SE OF IMAGES (dB)

	SNR=20dB	SNR=10dB	SNR=5dB
Proposal (case 1)	167.0	165.5	165.6
Proposal (case 2)	165.9	165.2	165.5
Proposal (case 3)	163.6	163.5	163.9
GAPES (case 1)	166.7	166.7	166.8
GAPES (case 2)	166.7	166.7	166.9
GAPES (case 3)	166.7	166.7	166.8

much higher TBRs than GAPES as one can note from Table II. High TBR indicates that the sparsity-driven method has prominent capability of denoising. In Table III, we list the signal energy of the reconstructed images. Generally, GAPES via images has identical signal energy, while the sparsity-driven approach generates images with lower signal energy, which indicates that to achieve the denoising performance, the sparsity-driven approach pays a price of some signal energy loss. However, loss of some weak scatters will not affect the geometrical construction of ISAR image, therefore we believe the sparsity-driven approach for SA-ISAR imaging is useful in real applications.

V. CONCLUSION

In this paper, we present a sparsity-driven algorithm to generate high-resolution ISAR images with sparse apertures, in which SA-ISAR imaging problem is converted into a sparsity-constrained optimization based on Bayesian compressive sensing. By using conventional Doppler tracking and autofocus, a two-step preprocessing for phase adjustment is developed to improve the efficiency and precision of the sparsity-constrained SA-ISAR imaging effectively. Real data experiments and the results manifest the effectiveness of the proposed approach in different conditions. For the issue of SA-ISAR imaging, there are still some open problems. For example, the SA imaging for maneuvering targets may be much involved, and distributed ISAR can also generate SA data with very short CPI [43], but the synchronization is a significant problem. They remain to be carried out in the future work.

ACKNOWLEDGMENT

The authors thank the anonymous reviewers for their valuable comments to improve the paper quality.

REFERENCES

[1] D. L. Mensa, *High Resolution Radar Imaging*. Dedham, MA: Artech House, 1981.
[2] W. G. Carrara, R. S. Goodman, and R. M. Majewski, *Spotlight Synthetic Aperture Radar-Signal Processing and Algorithms*. Boston, MA: Artech House, 1995.
[3] Q. Zhang and Y. Q. Jin, "Aspects of radar imaging using frequency-stepped chirp signals," *EURASIP J. Appl. Signal Process.*, vol. 2006, pp. 1–8, 2006, Article ID 85823.
[4] E. G. Larsson, G. Q. Liu, P. Stoica, and J. Li, "High-resolution SAR imaging with angular diversity," *IEEE Trans. Aerosp. Electron. Syst.*, vol. 37, no. 4, pp. 1359–1372, Oct. 2001.

[5] J. Salzman, D. Akamine, R. Lefevre, and J. C. Kirk, Jr., "Interrupted synthetic aperture radar (SAR)," *IEEE Aerosp. Electron. Syst. Mag.*, vol. 17, no. 5, pp. 33–39, May 2002.
[6] J. A. Hogbom, "Aperture synthesis with non-regular distribution of interferometer baselines," *Astron. Astrophys. Suppl.*, vol. 15, pp. 417–426, 1974.
[7] J. Tsao and B. D. Steinberg, "Reduction of sidelobe and speckle artifacts in microwave imaging: The CLEAN technique," *IEEE Trans. Antennas. Propag.*, vol. 36, no. 4, pp. 543–556, Apr. 1988.
[8] R. Bose, A. Freeman, and B. D. Steinberg, "Sequence CLEAN: A modified deconvolution technique for microwave images of contiguous targets," *IEEE Trans. Aerosp. Electron. Syst.*, vol. 38, no. 1, pp. 89–96, Jan. 2002.
[9] E. G. Larsson, P. Stoica, and J. Li, "Amplitude spectrum estimation for two-dimensional gapped data," *IEEE Trans. Signal Process.*, vol. 50, no. 6, pp. 1343–1353, Jun. 2002.
[10] E. G. Larsson, P. Stoica, and J. Li, "Spectral analysis of gapped data," in *Proc. 34th Asilomar Conf. Signals, Syst. Comput.*, 2000, vol. 1, pp. 207–211.
[11] E. G. Larsson and J. Li, "Spectral analysis of periodically gapped data," *IEEE Trans. Aerosp. Electron. Syst.*, vol. 39, no. 3, pp. 1089–1097, Jul. 2003.
[12] H. J. Li, N. H. Farhat, and Y. S. Shen, "A new iterative algorithm for extrapolation of data available in multiple restricted regions with applications to radar imaging," *IEEE Trans. Antennas. Propag.*, vol. AP-35, no. 5, pp. 581–588, May 1987.
[13] S. D. Cabrera and T. W. Parks, "Extrapolation and spectral estimation with iterative weighted norm modification," *IEEE Trans. Signal Process.*, vol. 39, no. 4, pp. 842–851, Apr. 1991.
[14] K. M. Cuomo, J. E. Piou, and J. T. Mayhan, "Ultrawide-band coherent processing," *IEEE Trans. Antennas Propag.*, vol. 47, no. 6, pp. 1094–1107, Jun. 1999.
[15] X. Xu and X. Feng, "SAR/ISAR imagery from gapped data: Maximum or minimum entropy," in *Dig. IEEE AP-S Int. Symp. URSI Meeting*, Washington, DC, Jul. 2005, vol. 4B, pp. 122–125.
[16] X. Xu, P. Huang, and X. Feng, "An iterative algorithm for ultra wideband radar imaging from randomly fragmented spectral data," in *Proc. SEE Radar Conf.*, France, Oct. 2004, pp. 668–671.
[17] D. E. Wahl, P. H. Eichel, D. C. Ghiglia, and C. V. Jakowatz, Jr., "Phase gradient autofocus—A robust tool for high resolution SAR phase correction," *IEEE Trans. Aerosp. Electron. Syst.*, vol. 30, no. 3, pp. 827–834, Jul. 1994.
[18] W. Ye, T. S. Yeo, and Z. Bao, "Weighted least-squares estimation of phase errors for SAR/ISAR autofocus," *IEEE Trans. Geosci. Remote Sens.*, vol. 37, no. 5, pp. 2487–2494, Sep. 1999.
[19] V. C. Chen and S. Qian, "Joint time-frequency transform for radar range-Doppler imaging," *IEEE Trans. Aerosp. Electron. Syst.*, vol. 34, no. 2, pp. 486–499, Apr. 1998.
[20] F. Berizzi and G. Cosini, "Autofocusing of inverse synthetic aperture radar images using contrast optimization," *IEEE Trans. Aerosp. Electron. Syst.*, vol. 32, no. 3, pp. 1185–1191, Jul. 1996.
[21] X. Li, G. S. Liu, and J. L. Ni, "Autofocusing of ISAR images based on entropy minimization," *IEEE Trans. Aerosp. Electron. Syst.*, vol. 35, no. 4, pp. 1240–1251, Oct. 1999.
[22] L. Zhang, M. Xing, C. Qiu, J. Li, and Z. Bao, "Achieving higher resolution ISAR imaging with limited pulses via compressed sampling," *IEEE Geosci. Remote Sens. Lett.*, vol. 6, no. 3, pp. 567–571, Jul. 2009.
[23] M. Çetin and W. C. Karl, "Feature-enhanced synthetic aperture radar image formation based on nonquadratic regularization," *IEEE Trans. Image Process.*, vol. 10, no. 4, pp. 623–631, Apr. 2001.
[24] N. O. Onhon and M. Çetin, "A nonquadratic regularization-based technique for joint SAR imaging and model error correction," in *Proc. SPIE, Algor. Synthetic Aperture Radar Imagery XVI*, 2009, vol. 7337, p. 73370C.
[25] A. C. Gurbuz, J. H. McClellan, and W. R. Scott, "A compressive sensing data acquisition and imaging method for stepped frequency GPRs," *IEEE Trans. Signal Process.*, vol. 57, no. 7, pp. 2640–2650, Jul. 2009.
[26] E. Candès, J. Romberg, and T. Tao, "Robust uncertainty principles: Exact signal reconstruction from highly incomplete frequency information," *IEEE Trans. Inf. Theory*, vol. 52, no. 2, pp. 489–509, Feb. 2006.
[27] E. Candès, J. Romberg, and T. Tao, "Near-optimal signal recovery from random projections: Universal encoding strategies?," *IEEE Trans. Inf. Theory*, vol. 52, no. 2, pp. 489–509, Feb. 2006.
[28] D. Donoho, "Compressed sensing," *IEEE Trans. Inf. Theory*, vol. 52, no. 4, pp. 5406–5425, Apr. 2006.
[29] S. Ji, Y. Xue, and L. Carin, "Bayesian compressive sensing," *IEEE Trans. Signal Process.*, vol. 56, no. 6, pp. 2346–2356, Jun. 2008.
[30] C. C. Chen and H. C. Andrews, "Target-motion-induced radar imaging," *IEEE Trans. Aerosp. Electron. Syst.*, vol. AES-16, no. 1, pp. 2–14, Jan. 1980.
[31] J. Wang and D. Kasilingam, "Global range alignment for ISAR," *IEEE Trans. Aerosp. Electron. Syst.*, vol. 39, no. 1, pp. 351–357, Jan. 2003.
[32] T. Sauer and A. Schroth, "Robust range alignment algorithm via Hough transform in an ISAR imaging system," *IEEE Trans. Aerosp. Electron. Syst.*, vol. 31, no. 3, pp. 1173–1177, Jul. 1995.
[33] D. Zhu, L. Wang, Y. Yu, Q. Tao, and Z. Zhu, "Robust ISAR range alignment via minimizing the entropy of the average range profile," *IEEE Geosci. Remote Sens. Lett.*, vol. 6, no. 2, pp. 204–208, Apr. 2009.
[34] S. S. Chen, D. L. Donoho, and M. A. Saunders, "Atomic decomposition by basis pursuit," *SIAM Rev.*, vol. 43, no. 1, pp. 129–159, 2001.
[35] H. Rohling, "Radar CFAR thresholding in clutter and multiple target situations," *IEEE Trans. Aerosp. Electron. Syst.*, vol. AES-19, no. 4, pp. 608–621, Jul. 1983.
[36] G. Davidson, "Matlab and c radar toolbox," 2003 [Online]. Available: http://www.radarworks.com
[37] C. W. Zhu, "Stable recovery of sparse signals via regularized minimization," *IEEE Trans. Inf. Theory*, vol. 54, no. 7, pp. 3364–3367, Jul. 2008.
[38] J. F. Sturm, "Using SeDuMi 1.02, a Matlab toolbox for optimization over symmetric cones," Tilburg Univ., Tilburg, The Netherlands, Tech. rep., Aug. 1998–Oct. 2001.
[39] D. L. Donoho, I. Driori, V. C. Stodden, and Y. Tsaig, "Sparselab," 2007 [Online]. Available: http://sparselab.stanford.edu/
[40] M. Grant, S. Boyd, and Y. Ye, "cvx: Matlab software for disciplined convex programming," 2011 [Online]. Available: http://www.stanford.edu/~boyd/cvx/
[41] C. R. Vogel and M. E. Oman, "Fast, robust total variation-based reconstruction of noisy, blurred images," *IEEE Trans. Image Process.*, vol. 7, no. 6, pp. 813–824, Jun. 1998.
[42] R. Acar and C. R. Vogel, "Analysis of bounded variation penalty methods for ill-posed problems," *Inverse Prob.*, vol. 10, pp. 1217–1229, 1994.
[43] D. Pastina, M. Bucciarelli, and P. Lombardo, "Multistatic and MIMO distributed ISAR for enhanced crossrange resolution of rotating Targets," *IEEE Trans. Geosci. Remote Sens.*, vol. 48, no. 8, pp. 3300–3317, Aug. 2010.

Lei Zhang was born in China in 1984. He received the B.S. degree in mechanism and electrical engineering from Chang'an University, Xi'an, China, in 2006, and is currently pursuing the Ph.D. degree in signal processing at the National Key Laboratory of Radar Signal Processing, Xidian University, Xi'an, China.

His major research interest is radar imaging (SAR/ISAR).

Zhijun Qiao (M'10) received the Ph.D. degree in applied math from the Institute of Mathematics, Fudan University, Shanghai, China, in 1997, wherein his dissertation was one of the first 100 excellent Ph.D. dissertations awarded in 1999.

From 1999 to 2001, he was a Humboldt Research Fellow with the Department of Mathematics and Computer Science, University of Kassel, Kassel, Germany. From 2001 to 2004, he was a Researcher with the Theoretical Division, Los Alamos National Laboratory, Los Alamos, NM. He was also a Professor with the Department of Mathematics, Liaoning University, Shenyang City, China, since 1997. Currently, he is the PI of two grants under the Department of Defense program and the Norman Hackerman Advanced Research Program. He is currently with the Department of Mathematics, The University of Texas-Pan American, Edinburg. He is currently the Editor-in-Chief of the *Pacific Journal of Applied Mathematics*. He has published two monographs and more than 90 articles in peer-reviewed international journals. His research interests include nonlinear partial differential equations and its application in radar imaging.

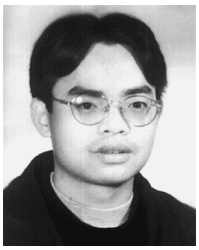

Mengdao Xing (M'04) was born in China in 1975. He received the Bachelor's and Ph.D. degrees in electrical engineering from Xidian University, Xi'an, China, in 1997 and 2002, respectively.

He is currently a Full Professor with the National Key Laboratory for Radar Signal Processing, Xidian University. His research interests include SAR, ISAR, and over-the-horizon radar (OTHR).

Jialian Sheng was born in China in 1987. She received the B.S. degree in electrical engineering from Xidian University, Xi'an, China, in 2010, and is currently pursuing the Ph.D. degree in signal processing at the National Laboratory for Radar Signal Processing, Xidian University.

Her major research interests are radar signal processing and radar imaging.

Rui Guo was born in China in 1985. She received the B.S. degree in electrical engineering from Xidian University, Xi'an, China, in 2007, and is currently pursuing the Ph.D. degree in signal processing at the National Laboratory for Radar Signal Processing, Xidian University.

Her major research interests are radar imaging and image processing, especially polarimetric synthetic aperture radar.

Zheng Bao (M'80–SM'90) was born in Jiangsu, China. He received the Bachelor's degree in radar engineering from Xidian University, Xi'an, China, in 1953.

He is currently a Professor with Xidian University and the Chairman of the Academic Board of the National Key Laboratory of Radar Signal Processing. He has authored or coauthored six books and published over 300 papers. Currently, his research fields include space-time adaptive processing (STAP), radar imaging (SAR/ISAR), automatic target recognition (ATR) and over-the-horizon radar (OTHR) signal processing.

Prof. Bao is a member of the Chinese Academy of Sciences.